Article

Forward Modeling Simulations to Validate Changes in Electrical Resistivity Tomography Monitoring Data for a Slope with Complex Geology

Azadeh Hojat [1,2], Luigi Zanzi [1,*], Greta Tresoldi [3] and Meng Heng Loke [4]

[1] Dipartimento di Ingegneria Civile e Ambientale, Politecnico di Milano, 20133 Milan, Italy; azadeh.hojat@polimi.it or ahojat@uk.ac.ir
[2] Department of Mining Engineering, Shahid Bahonar University of Kerman, Kerman 76188, Iran
[3] LSI LASTEM, 20049 Settala, Italy; greta.tresoldi@lsi-lastem.com
[4] Geotomo Software Sdn Bhd, Gelugor 11700, Malaysia; drmhloke@gmail.com
[*] Correspondence: luigi.zanzi@polimi.it

Abstract: The electrical resistivity tomography (ERT) method has been increasingly integrated with hydrogeological risk mitigation strategies to monitor the internal conditions and the stability of natural and artificial slopes. In this paper, we discuss a case study in which numerical simulations were essential to validate the interpretation of the resistivity images obtained from an ERT monitoring system installed on a critical slope in Italy. An initial analysis of the monitoring data after rainfall events in the study site showed that the resistivity values were decreased only in the central zone along the ERT line, but they were increased in the two sides of the profile. Opposite behaviors were observed during the drying processes following the rainfall events. Core samples show complex geology at the study site, which might justify uneven responses of the different subsurface bodies to meteorological events. However, we decided to investigate the possible inversion artifacts resulting from the individual inversion of the tomographic sections. Forward modeling simulations on simplified time-lapse models of the study site were performed to explore this problem and to compare the individual and time-lapse inversions. Synthetic tests confirmed the nature of these unexpected behaviors and assessed the absolute necessity of a time-lapse approach for a correct inversion of monitoring data in the presence of a complex geological model such as the one of this case study. By applying the time-lapse inversion approach to the real data, the inversion artifact problem was substantially solved, arriving after the proper calibration of the inversion parameters, mainly the time-lapse damping factor and the spatial and temporal roughness constraints, to a reduction in the inversion artifacts to less than 5%.

Keywords: hydrogeological risk mitigation; slope stability; ERT monitoring; time-lapse inversion; time-lapse damping factor; water content

1. Introduction

In recent years, geophysical monitoring systems have increasingly helped in real-time monitoring of unstable slopes to minimize the impact of hazardous events—e.g., [1–15]. The main objective of all geophysical monitoring systems is to keep an eye on the parameters that might result in the instability conditions of the slope (e.g., fracture development, excess water saturation) as well as to improve the early-warning alarming strategies. Therefore, time-lapse data acquisitions permit evaluating the time variations in the critical parameters responsible for instability before failure occurrence.

One critical parameter to be monitored in hydrogeological risk mitigation studies is the subsurface water content. Among the non-invasive sensing technologies, the electrical resistivity tomography (ERT) method is one of the most efficient geophysical techniques to map the saturation degree of water and other liquids in the vadose zones [16–21]. The possibility to calibrate site-dependent formulations between the electrical resistivity and water content of a material is the main reason that the ERT monitoring method is increasingly used to monitor natural and artificial slopes—e.g., [1–3,7,22–27].

The measured data in an ERT survey are the apparent resistivity values that will then undergo an inversion approach to obtain the real resistivity values of the subsurface. The inversion algorithm searches for a model of the subsurface resistivity distribution for which the calculated model response matches the measured apparent resistivity values [26,28]. The final goal of integrating an ERT monitoring system with hydrogeological risk mitigation strategies is to transform the final resistivity model into water content maps and define thresholds of alarm. Therefore, it is crucial to invert the ERT monitoring data as free as possible from inversion artifacts in order to correctly interpret the results and define thresholds of instability [23]. In this paper, Res2dinvx64 software ver. 2024.2 (Copyright © Seequent Systems, Incorporated, Christchurch, New Zealand) was used for inverting ERT data. In order to adequately model different subsurface structures including complex resistivity distributions, Res2dinvx64 uses a cell-based inversion technique that subdivides the subsurface into rectangular cells with fixed sizes and positions [29]. The inversion algorithm starts from an initial model that is normally a homogeneous half-space using the average measured apparent resistivity values. This is the most general model as it does not make any assumptions about the resistivity distribution and therefore, it is less likely to bias the final inversion model. A finite-element or finite-difference modeling subroutine can be employed to calculate the apparent resistivity values, and the resistivity of the model blocks is calculated using a non-linear smoothness-constrained least-squares optimization technique [30,31]. A local optimization method is normally used for practical reasons. A global optimization method takes days to weeks even for a single non-time-lapse dataset [32]. While global optimization methods avoid the problem of local minima, they are at present not practical to use for real-time monitoring problems where several datasets might be acquired in a single day.

Similar to other geophysical problems, the ERT inverse problem is inherently non-linear and ill-posed, resulting in different model parameters that produce almost the same experimental observations [28,29,32,33]. In this paper, we present the problem of suspected inversion artifacts in resistivity sections for a permanent ERT monitoring system that is in operation from March 2022 on an important slope in Italy. The problem arose after the first rainfall events occurring after installing the ERT system in the study site when we expected that the resistivity of the shallow subsurface would decrease with time along the profile. However, it was observed that the resistivity decreased only in the central zone of the profile and considerably increased in the side parts of the profile. Through synthetic modeling, we demonstrate that this unexpected behavior is due to inversion artifacts and we show how these artifacts can be drastically attenuated by applying a time-lapse inversion procedure with optimal setting of the constraining parameters.

2. The Case Study

The case study is a critical slope above an important infrastructure tunnel in Italy. Reconnaissance ERT measurements were performed along two parallel lines covering the full available length. An IRIS Syscal Pro instrument supporting 96 electrodes was used and different electrode configurations including the Wenner, the Wenner–Schlumberger, and the dipole–dipole arrays with the unit electrode spacing of 2 m were used for the

preliminary surveys. Based on the results of reconnaissance surveys and discussions with the authorities managing the study site, a 2D ERT profile using the Wenner electrode configuration with unit electrode spacing of 3m was permanently installed in March 2022. Figure 1a illustrates a picture of deploying the cables (protected by a robust anti-rodent cover) connected to plate electrodes and buried inside a 0.4 m deep trench. Figure 1b shows the central part of the ERT profile where the box containing the electronics of the system and the battery is positioned. The customized ERT monitoring system supports two 24-electrode cables and is accompanied by a weather station including a rain gauge and a thermohygrometer and they are all powered by a solar panel. For seasonal analysis of the annual data, a temperature sensor was also installed at the depth of 1.5 m to monitor the variations in the soil temperature.
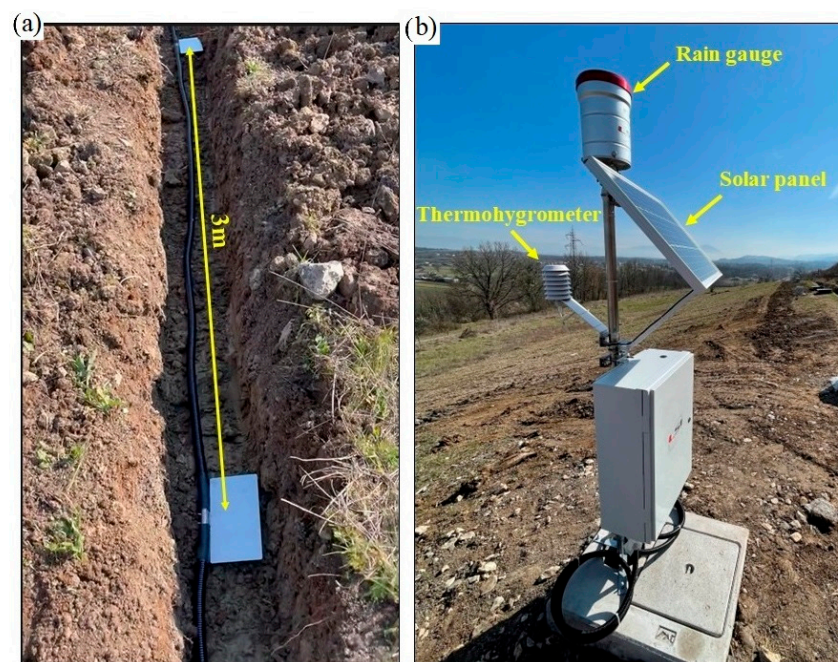

Figure 1. The customized ERT monitoring system installed in the study site: (**a**) Protected cables and plate electrodes with the spacing of 3 m are buried inside a trench at the depth of 0.4 m. (**b**) The box containing the electronics and the battery is positioned in the middle of the ERT profile along with the weather station and a solar panel.

Core samples were also taken at five points along the ERT line and the geological model of the study site was reconstructed as shown in Figure 2. The boreholes were located with almost equal distances of about 15 m and cores were recovered down to 20 m in each borehole. Figure 2 shows a complex subsurface geology at the study site with both horizontal and vertical changes. Analysis of the core samples and the preliminary ERT surveys could detect a zone with considerably higher permeability. This zone is positioned in the central part along the permanent ERT monitoring line where the core stratigraphy indicates a large presence of calcareous gravels. The site is also characterized by a thin superficial clayey layer inside which the electrodes of the permanent ERT system were deployed to ensure low contact resistances. Note also another thin layer at the base of the brown-whitish topsoil, classified as a brown-grayish alteration of Chaotic Clays, which shows a remarkable thickness increase in the fourth borehole.
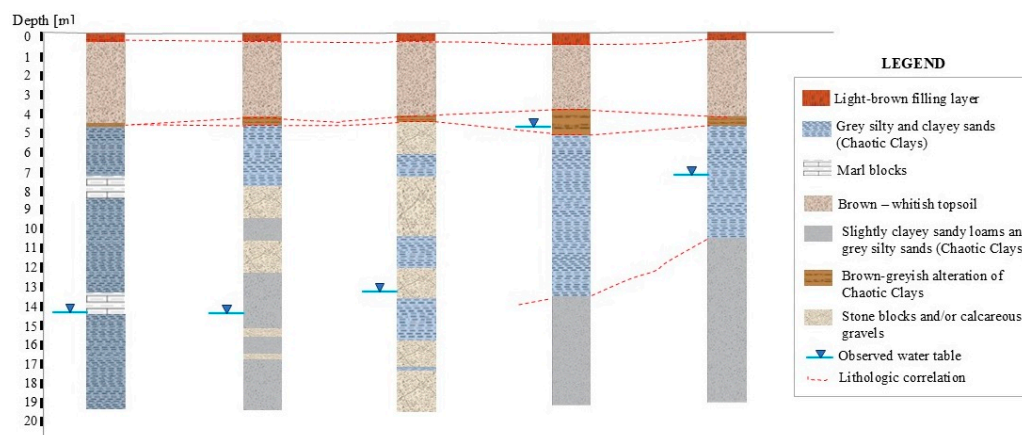
Figure 2. The geological model and the piezometric levels defined from the core samples recovered in five boreholes along the ERT profile.

3. Inversion of ERT Monitoring Data

We used Res2dinvx64 software for all ERT inversions (either individual or time-lapse inversions) discussed in this paper. The only exception is Figure 9a that presents the results of inversions obtained by the cloud software of the ERT monitoring system. Most of the inversion parameters were set up accepting the default values used by Res2dinvx64. The maximum number of iterations was set to 11 but the inversion algorithm normally converged in 6 iterations with an absolute error lower than 5–6%. An ERT inversion algorithm tries to find a model for which the calculated apparent resistivity values (using a finite-difference or a finite-element subroutine) fit the measured data within a reasonable error. The regularized least-squares optimization method is the most common inversion technique to reconstruct the arbitrary subsurface resistivity distribution from ERT data [29]. Two of the most common constraints used in the regularized least-squares optimization method are the robust/blocky method (L1 norm) and smooth method (L2 norm). The robust/blocky inversion method gives optimal results for models with sharp transitions in resistivity values while the smooth inversion method results in an inversion model with smooth variations in the subsurface resistivity [29].

ERT monitoring data are normally inverted using a time-lapse algorithm. There are two main classes of time-lapse inversion algorithms using either the older ratio or difference method [34] or the newer temporal smoothness-constrained method [35]. The difference method is normally used with only two datasets at a time (the initial dataset and one later-time dataset) and uses the difference or ratio of the apparent resistivity values. As far as the authors know, the inversion is limited to time series with only two sets of measurements at a single time and in case of having more than two datasets, we suppose that multiple separate inversions are carried out using the initial dataset and one of the later-time datasets. On the other hand, the newer temporal smoothness-constrained method is more difficult to implement but it has the advantage of being more flexible. The method can be used to invert more than two sets of measurements at a single time [35,36]. The second advantage is that the nature of the changes in resistivity values between the time-lapse models can be modified using the temporal roughness filter, i.e., whether considering the normal L2 norm with gradual changes in time or the L1 norm with abrupt/blocky changes in time. Moreover, many other modifications are also possible, such as concentrating the changes in selected areas where more information is available [37] or setting the changes to only

increase or decrease with time [36]. The time-lapse smoothness-constrained least-squares optimization method is described by Equation (1) [38]:

$$[J_k^T R_d J_k + \left(\lambda W^T R_m W + \alpha M^T R_t M\right)]\Delta r_k = J_k^T R_d g_k - \left(\lambda W^T R_m W + \alpha M^T R_t M\right) r_{k-1} \quad (1)$$

where J is the Jacobian matrix that contains the partial derivatives of the apparent resistivity values with respect to the model resistivity values (r); k is the iteration number; W is the spatial roughness filter matrix; M is the temporal roughness filter; g is the data misfit vector; R_d, R_m, and R_t are weighting matrices used by the L1-norm inversion method [38]; λ is the spatial damping factor vector; and α is the temporal damping factor, which controls the relative importance given to minimize the difference between models at different times.

ERT monitoring systems managed by our team are mainly installed along earthen embankments like river levees and tailings dams—e.g., [25] with homogenous material. One exception is the monitoring site along a river levee in Colorno, Italy, where there is a lateral inhomogeneity due to levee repair [39]. For all these sites, we initially compared individual versus time-lapse inversion of ERT data and the results were completely similar thanks to non-complex subsurface conditions. For the study site presented in this paper, on the other hand, we noticed that suspected artifacts appeared in the results after the beginning of rainfalls or dry periods when the data were inverted individually. Figure 3 illustrates an example of such inversion results for the data measured on 30–31 March 2022 before and after a rain event. This was the first rainfall event in the study site after installing the ERT monitoring system. We know that the subsurface material in the lateral zones along the ERT profile are composed of clay and thus, water infiltration would be much slower in these parts compared to the higher-permeable central part. In any case, we expect the resistivity values to be decreased along the whole profile on 31 March 2022 after the rainfall. Instead, we observe that the resistivity is only decreased (more than 50%) in the central zone and meaningless increases occur in the resistivity values of the side zones, approaching more than 20% on the right side. This is opposite to what should be observed after a rainfall event and the suspected artifacts might be favored by the complex subsurface geology of the study site. Opposite trends in the central and side zones of the ERT profile were observed after one or two days of no rain. Instead of observing the resistivity values to be increased along the whole profile, we observed that the resistivity values were decreased in the side zones and only increased in the central part.
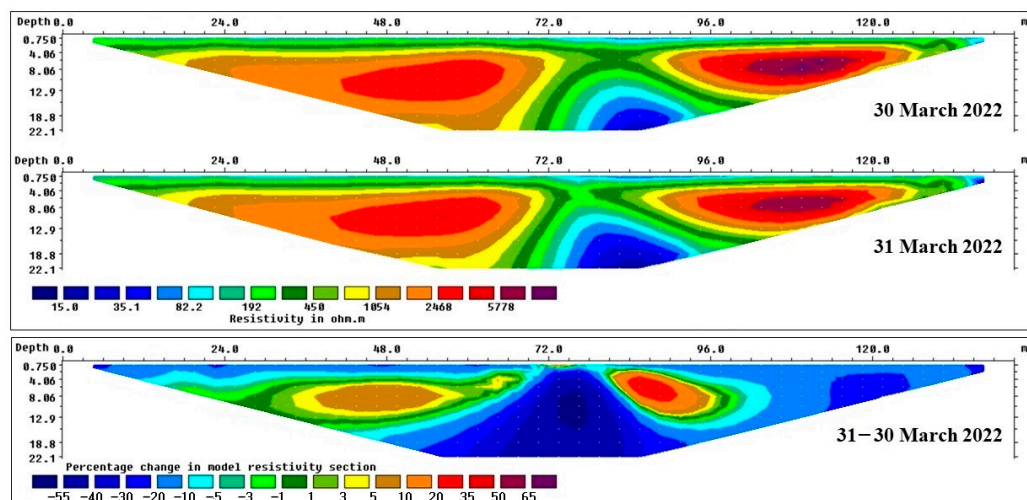

Figure 3. An example of inversion results from the individual inversion of datasets measured on 30 and 31 March 2022 before and after a rain event, respectively.

3.1. Synthetic Tests

In order to investigate the problem, we defined a simplified geological model of the study site on which we performed synthetic tests to compare individual versus time-lapse inversions. The synthetic models of the study site (Figure 4) were defined in Res2dmod (geotomosoft.com) [40] and the synthetic time-lapse ERT data were then generated for these models. In order to be compatible with the ERT monitoring data in the study site, the synthetic data were generated for the Wenner electrode configuration using 48 electrodes with the unit electrode spacing of 3 m.
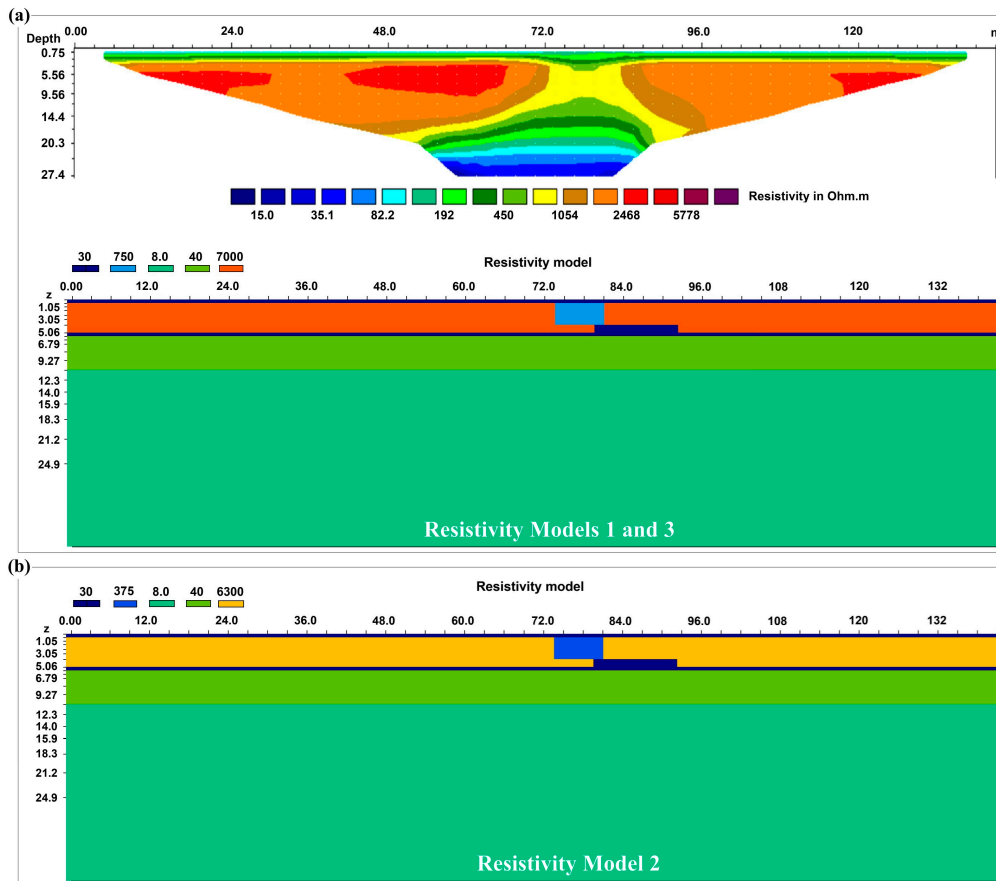

Figure 4. Simplified time-lapse synthetic models of the study site. (**a**) Models 1 and 3 for the initial model (defined based on coring data and resistivity values measured on samples in the laboratory) and the return of Model 2 to Model 1 (after the rainfall stopped for a few days and the resistivity was increased along the whole profile), respectively. The top image was obtained by inverting the synthetic data calculated on the model. (**b**) Model 2 simulates the situation after a rainfall event with resistivity values of the sand and gravel layer decreased along the whole profile (50% in the central zone and 10% in side zones).

Model 1 illustrated in Figure 4a simulates an initial condition. This model is a simplified layered model defined based on Figure 2. We remind that the purpose of synthetic tests was only validating the presence of artifacts caused by individual inversions, and the defined simplified model was shown to be adequate for this purpose. The resistivity values are selected according to laboratory measurements performed on some selected samples taken along the ERT line and at different depths. According to Model 1, the study site is characterized by 0.5 m of a thin superficial clayey layer with the resistivity of 30 Ωm. This superficial layer rests on a 4 m thick layer of dry sand and gravel with the resistivity of 7000 Ωm. One important characteristic of the second layer is the presence of an anomalous central zone with considerably higher porosity and permeability. The resistivity of this

central anomalous part is about 750 Ωm in dry conditions. The third layer in Model 1 is another 0.5 m thick clay layer with the resistivity of 30 Ωm. As shown in the geological model (Figure 2), the third layer becomes thicker in the central part of the profile. We thus define a thicker part for this layer from about 80 m to 93 m along the x axis in the synthetic model (Figure 4). More complexity is observed for deeper layers in the real geological model (Figure 2), but we simplified the deeper parts of the synthetic model, defining a fourth layer with the resistivity of 40 Ωm down to about 10.5 m. For what concerns the depth-to-water table in the study site, complex behavior is observed as well (Figure 2) with some piezometers measuring values as deep as about 13–14 m and a couple of piezometers observing the water table as shallow as 4–5 m. Again, we simplified the synthetic model defining the deepest layer to be below the water table for the full length of the ERT profile and it is defined with the average resistivity of 8 Ωm. The inversion result for the synthetic data calculated on Model 1 is also shown in Figure 4a. A comparison of this inverted image with the examples of the inversion results shown in Figure 3 validates the model for the purpose of this simulation since it shows that the defined synthetic model, although simplified, is a proper representation of the main characteristics of the study site.

In order to define time-lapse synthetic models, Model 2 in Figure 4b simulates an expected situation after a rainfall event. Considering that the central part of the profile has a higher permeability, a rapid decrease of 50% in resistivity is modeled for this zone while a slower decrease of 10% happens in less-permeable lateral parts of the sand and gravel layer. The third model is defined to simulate a dry period and show the return to the initial model after the rainfall stopped for a few days. Thus, compared to Model 2, the resistivity values of the shallow layers in Model 3 are increased along the whole profile and the subsurface returns to the initial situation. Therefore, Model 3 is actually Model 1 and it is exactly the model shown in Figure 4a.

Synthetic data calculated on the models illustrated in Figure 4 were then inverted in Res2dinvx64 software both individually and using the time-lapse algorithm. The results showed that the problem of suspected inversion artifacts described in Section 3 was also present when the synthetic data were individually inverted. As an example, Figure 5 illustrates the percentage resistivity changes for the resistivity images obtained using the smooth inversion method in the x-z directions and independent inversions in the time direction (singular inversion of each dataset). Figure 5a shows the percentage resistivity changes between Model 2 and Model 1, i.e., how the resistivity values changed after the rainfall. What we simulated is that going from Model 1 to Model 2 (Figure 4), the resistivity values in the shallow layers decrease along the whole profile, but we observe significant inversion artifacts in Figure 5a. The resistivity values are decreased in the central part of the profile but the resistivity decrease is extended to the deepest parts as well as to the left deep part of the image rather than occurring only in the shallow parts. Similar to field data, the other important artifact is that instead of observing the 10% decrease in the two sides of the profile for the shallow layers, we observe that the resistivity values are increased by about 10% in the lateral zones. Similarly, what we simulated for a drying period after rain going from Model 2 to Model 3 is that the resistivity increases in the shallow layers along the whole profile. Instead, Figure 5b shows how inversion artifacts produce exaggerated resistivity increases in the deep central and left zones rather than also modeling the increase in the shallow two sides of the profile. These two side zones show misleading decreases of more than 5% instead.
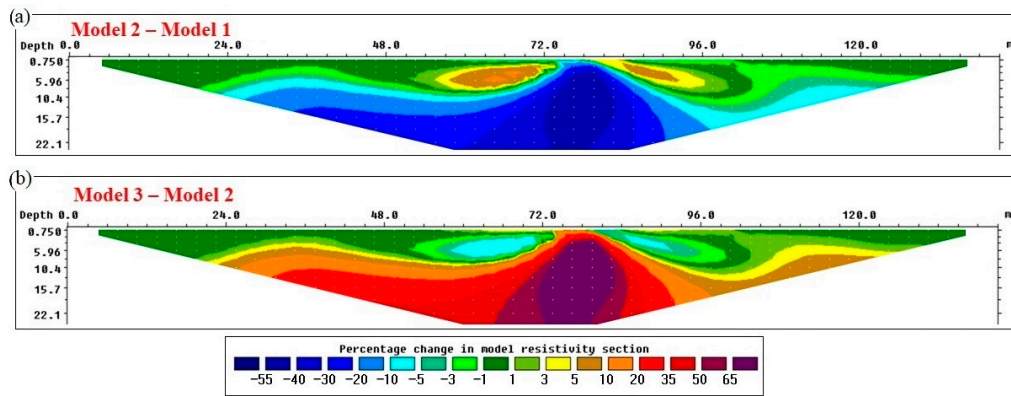
Figure 5. Percentage changes in resistivity sections obtained by the individual inversion of the synthetic data calculated on the models defined in Figure 4. (**a**) Resistivity changes after a rainfall event: Model 2−Model 1. (**b**) Resistivity changes after a dry period: Model 3−Model 2.

Forward modeling tests confirmed the presence of significant inversion artifacts when individually inverting the data. Time-lapse synthetic data were then inverted using the time-lapse inversion algorithm, exploring optimal parameters that could give reasonable results. We explored different parameters and the main parameter that showed remarkable benefits was the time-lapse damping factor, which is the cross-time model damping factor. The suggested common range for this parameter in Res2dinvx64 is 0.5–5. We tried different values for the time-lapse damping factor, observing that the results were considerably improved using values close to 5. However, some other inversion options also showed some beneficial influence on the results. One of these options is the type of the constraint in the time direction used in the time-lapse inversion. This temporal roughness constraint takes into consideration how the resistivity model for the later-time dataset is related to the model for the preceding dataset. We tried the options for the smooth changes and the robust/blocky changes for the temporal roughness constraint, which, respectively, ensures that time changes in the resistivity values of the corresponding model blocks are smooth or blocky. Finally, it was important to integrate the time-lapse damping factor and the temporal roughness constraint with the optimal inversion method in the space dimension, i.e., the robust/blocky inversion or the smooth inversion for the changes in the model resistivity in the x-z directions [29]. Examples of the inversion results for the synthetic data calculated on the models illustrated in Figure 4 using different spatial roughness constraints in x-z directions are shown in Figures 6 and 7 using the smooth inversions and the robust/blocky inversions, respectively.

Comparing Figure 6a with Figure 6b,c, we can notice the benefit of increasing the time-lapse damping factor to reduce the artifacts. As the time-lapse damping factor is increased from 1, the problem of the non-real extension of negative changes after the rainfall (Model 2−Model 1) or the positive changes during the drying period after the rainfall (Model 3−Model 2) is better resolved. Moreover, Figure 6a is hardly approaching the zero changes in deeper layers. Figure 6b,c can better reconstruct the zones with zero changes in depth, but neither of these images are still ideal. While the resistivity decrease in side zones is better approaching the modeled value in Figure 6b, the image is suffering more from the depth extension of the changes compared to Figure 6c. We also explored the effect of the temporal roughness constraint. Figure 6c,d were both produced using the smooth inversion method as the spatial roughness constraint and using the time-lapse inversion damping factor 5. The only difference is the temporal roughness constraint, using the blocky time constraint in Figure 6c and the smooth time constraint in Figure 6d. We can clearly observe the benefit of using the blocky changes in the time direction because

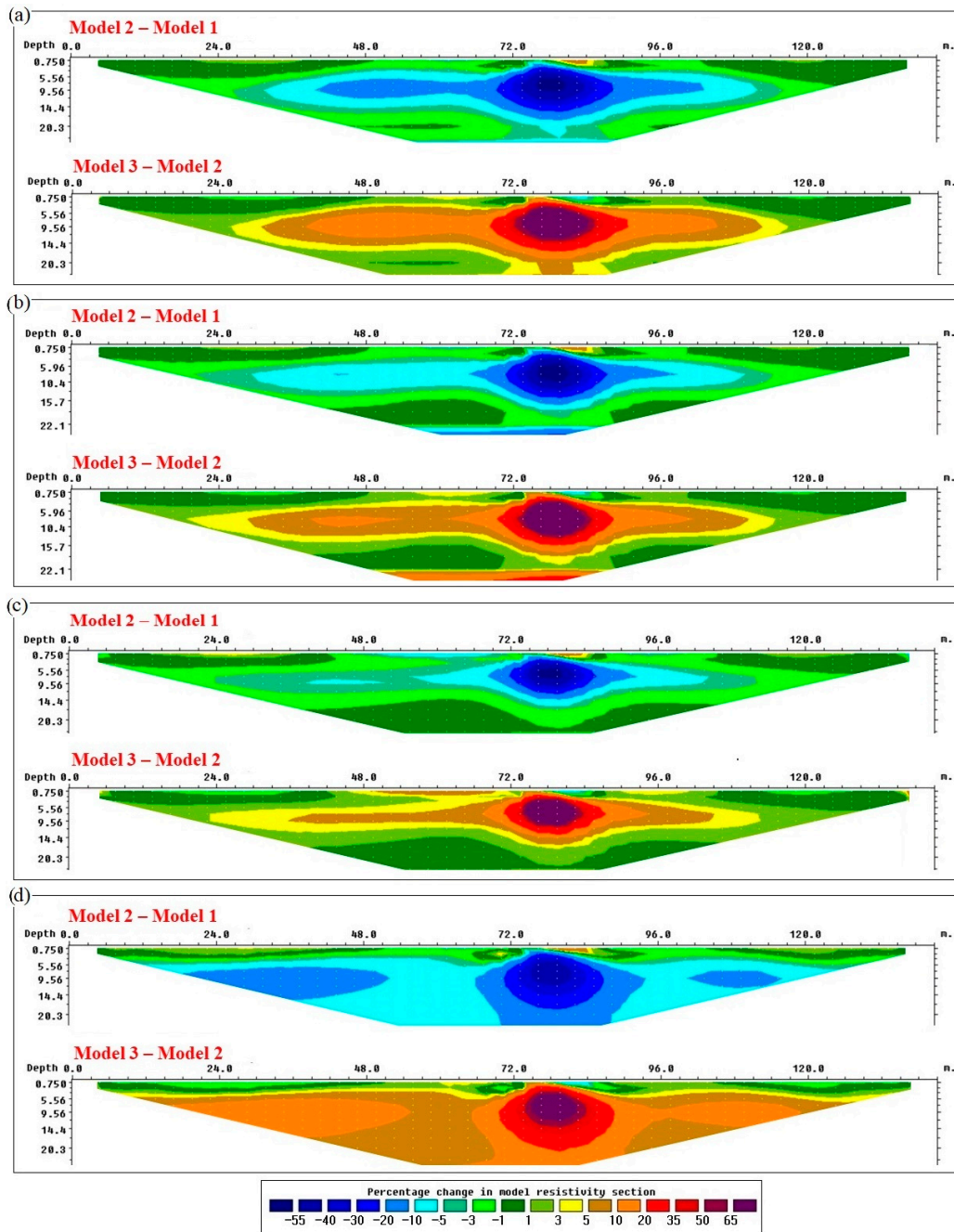significant artifacts remain when using the smooth constraint for the temporal roughness constraint (Figure 6d).

Figure 6. The time-lapse inversion of the synthetic data calculated on the models illustrated in Figure 4 using the smooth inversion method for the spatial roughness constraint: (**a**) time-lapse damping factor 1 and blocky temporal roughness constraint, (**b**) time-lapse damping factor 3 and blocky temporal roughness constraint, (**c**) time-lapse damping factor 5 and blocky temporal roughness constraint, (**d**) time-lapse damping factor 5 and smooth temporal roughness constraint.

The tests described in Figure 6 showed the benefit of combining a large time-lapse damping factor (3–5) with the option of blocky changes in the time direction, but the results are not still ideal. We then tried similar tests using the robust/blocky inversion method in the x and z directions. Figure 7 shows a couple of examples obtained using the time-lapse damping factor 5 and the robust/blocky inversion method in space. Figure 7a was obtained using the smooth temporal roughness constraint while Figure 7b was obtained using the

blocky changes as the temporal roughness constraint. Similar to what we observed in Figure 6, the benefit of using the blocky changes in the time direction is again highlighted in these tests. The difference images obtained using the smooth temporal roughness constraint are still suffering from misleading artifacts, mainly large changes exceeding +10% in deep layers. A comparison of Figure 7b with Figure 6b,c, on the other hand, underlines the benefit of using the robust/blocky inversion method in the space, which improves the similarity of the expected changes as modeled in Figure 4. In conclusion, it was observed that using the smooth inversion method in the space domain was not proper for the synthetic tests while satisfactory results could be obtained using the robust/blocky method in space. Figure 7b shows the benefit of using the robust/blocky method in x-z directions combined with the blocky changes in the time direction and tuning the time-lapse inversion damping factor, altogether causing the artifacts to be minimized and the solution to show the best fitting with the models of Figure 4.
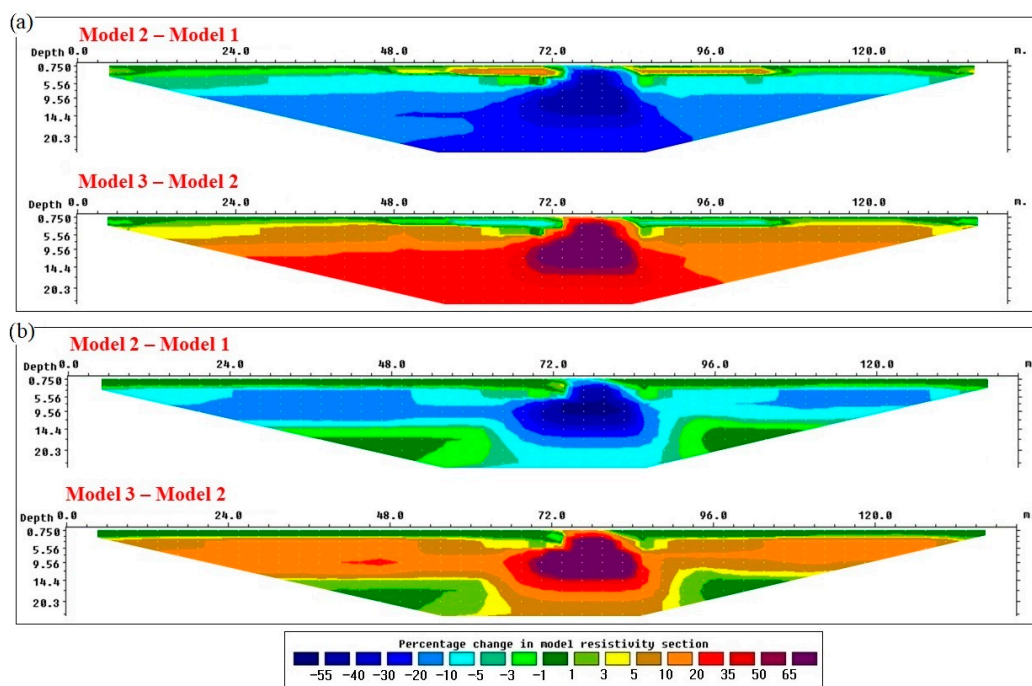

Figure 7. The time-lapse inversion of the synthetic data calculated on the models illustrated in Figure 4 using the robust/blocky inversion method for the spatial roughness constraint: (**a**) time-lapse damping factor 5 and smooth temporal roughness constraint, (**b**) time-lapse damping factor 5 and blocky temporal roughness constraint.

3.2. Field Data

Once the problem of inversion artifacts was well studied through forward modeling simulations, we moved towards the time-lapse inversion of field data. We focused on optimizing the time-lapse inversion parameters that were found to be the most influential in synthetic tests. Time-lapse inversion parameters were tested on datasets obtained in the first few months of the monitoring period to be sure to remove the artifacts as efficiently as possible. The monitoring system calculates the standard deviation of each measurement as a control on the error in datasets. The standard deviation was mostly less than 0.5% with the maximum of 1.9% for a couple of measurements for datasets used in this paper. Similar to synthetic datasets, optimal results for the time-lapse inversion of field data were obtained using a time-lapse damping factor equal to 5 and selecting the blocky changes for the temporal roughness constraint. However, different to synthetic simulations, the best results for field data were obtained using the smooth inversion method for the spatial

roughness constraint. Later in the following section, we will discuss more details on this issue.

As an example, Figure 8 illustrates optimal time-lapse inversion for the data measured before and after the first rainfall event after installing the ERT monitoring system in the study site. Compared to Figure 3, which presents the same data with inversion artifacts, Figure 8 now presents the realistic changes in resistivity values after a rainfall event. We can now observe realistic resistivity changes that show a reduction of about 20% in the shallow parts along the whole profile. Deeper layers show smaller changes due to a slower penetration of rain water at depth, but the resistivity variations always remain negative. We observe the most important changes with resistivity reductions larger than about 50% in the higher-permeable zone in the middle part of the profile. All these changes reflect a realistic situation compared to the strange variations observed in Figure 3.
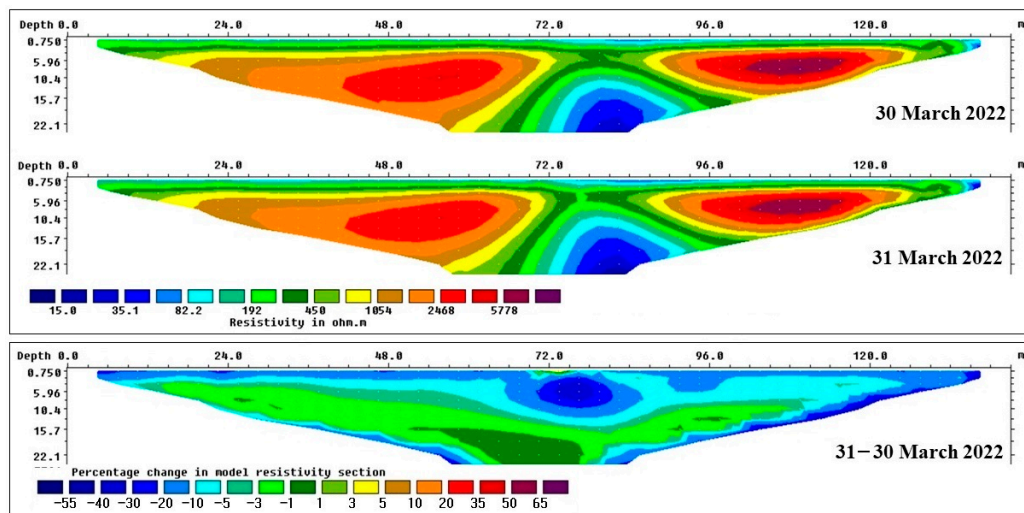

Figure 8. The results of the time-lapse inversion of monitoring data in the study site for datasets measured on 30 and 31 March 2022 (compare with Figure 3), before and after a rain event.

4. Discussion

While some studies are reported where minor differences are observed between individual or time-lapse inversions of long-term ERT monitoring data, several cases are also available where a time-lapse inversion algorithm is necessary to avoid artifacts [35]. This is because a standard inversion approach does not include any constraints on resistivity changes in the time direction. The study site presented in this paper is one such case where the complex subsurface geology resulted in the production of significant inversion artifacts when using individual or non-optimal time-lapse inversion algorithms for the ERT monitoring data. The subsurface material has a considerably higher permeability in the central zone along the ERT line compared to the lateral zones. Therefore, although we expect that resistivity changes with time would have the same sign along the whole ERT profile (i.e., decrease after rainfalls and increase after dry periods), the large resistivity contrasts in the central part result in the production of artifacts in temporal images [26]. This problem was explored in depth through synthetic simulations. According to the time-lapse synthetic models defined in Figure 4, the resistivity is decreased along the whole profile after a rainfall event. The modeled changes are 50% decrease in the central zone for the higher-permeable part and 10% decrease in less permeable lateral zones, but the artifacts generated by the individual inversions show up to 9% of an increase in the resistivity of the lateral zones (Figure 5a). A similar problem happened after simulating a dry period when we expect all resistivity values to be increased (100% in the central zone and 11% in lateral

zones), but Figure 5b shows that the inversion artifacts are produced in the lateral sides of the model where we observe a decrease with time rather than an increase in resistivity.

We compared singular versus time-lapse inversions of the synthetic time-lapse data. The synthetic tests were important in validating the presence of inversion artifacts caused by individual inversions and they proved the necessity of using a time-lapse inversion algorithm. The tests also showed the importance of optimizing the time-lapse inversion parameters, mainly the time-lapse damping factor and the temporal and space roughness constraints, to produce reliable images and to correctly interpret the results. However, the synthetic tests were not aimed at finalizing optimal time-lapse inversion parameters, because we had defined a simplified layered model of the real study site and we had used sharp changes between different vertical and horizontal boundaries for synthetic tests. Therefore, the robust/blocky inversion method for the spatial roughness constraint was more suitable for synthetic simulations to reconstruct the models with homogeneous regions separated by sharp boundaries [28]. For the real data, on the other hand, we expect a smooth subsurface resistivity distribution in the horizontal and vertical directions rather than sharp boundaries. As a result, the best inverted images were obtained using the smooth inversion method for the spatial roughness constraint that gives better results for gradual changes in subsurface resistivities [28]. For the type of the constraint in the time direction, the best results were obtained using the blocky temporal roughness constraint regardless of the type of the spatial roughness constraint (smooth method for field data and robust/blocky method for synthetic data).

The optimized time-lapse inversion parameters are continuously used to invert the datasets measured by the monitoring system. For more than 95% of datasets acquired from March 2022 to the time of writing this paper, the time-lapse inversion resulted in meaningful and artifact-free resistivity maps. As an example, Figure 9 illustrates the trends of average resistivity variations for successive days in the period 25 March–29 April 2022 compared to the rainfalls accumulated in the 24 h prior to each measurement. The graphs presented in Figure 9a are plotted from the individual inversions of datasets using the cloud software of the monitoring system while the graphs shown in Figure 9b are obtained from optimal time-lapse inversions performed in Res2dinvx64 software. Three types of resistivity variations are illustrated on the graphs shown in Figure 9: the average variations in all resistivity values distributed in the section, which indicate the sign and the amount of the dominant variation; the average positive variations in resistivity values, which are expected to be null after rainfalls and to be dominant during dry periods; and the average negative variations in resistivity values, which are expected to be null during dry periods and to be dominant after rainfalls. Comparing the trends of average resistivity changes with rainy and dry periods in Figure 9a with Figure 9b, we can observe how effectively the inversion artifacts are minimized to less than 3% (occurring on 31 March, after an important rainfall) using optimal time-lapse inversions. The trends of average variations in all resistivity values distributed in the section are well correlated with rainfalls or dry periods for the graphs shown in Figure 9b. As expected, these average resistivity changes and the average positive variations follow similar trends after dry periods while the trend is similar for the average resistivity changes and the average negative variations after rainfalls. On the contrary, in Figure 9a, we observe remarkable artifacts, especially positive variations after rainfalls, which affect the behavior of the total resistivity variations, demonstrating that their extension and intensity are not negligible.
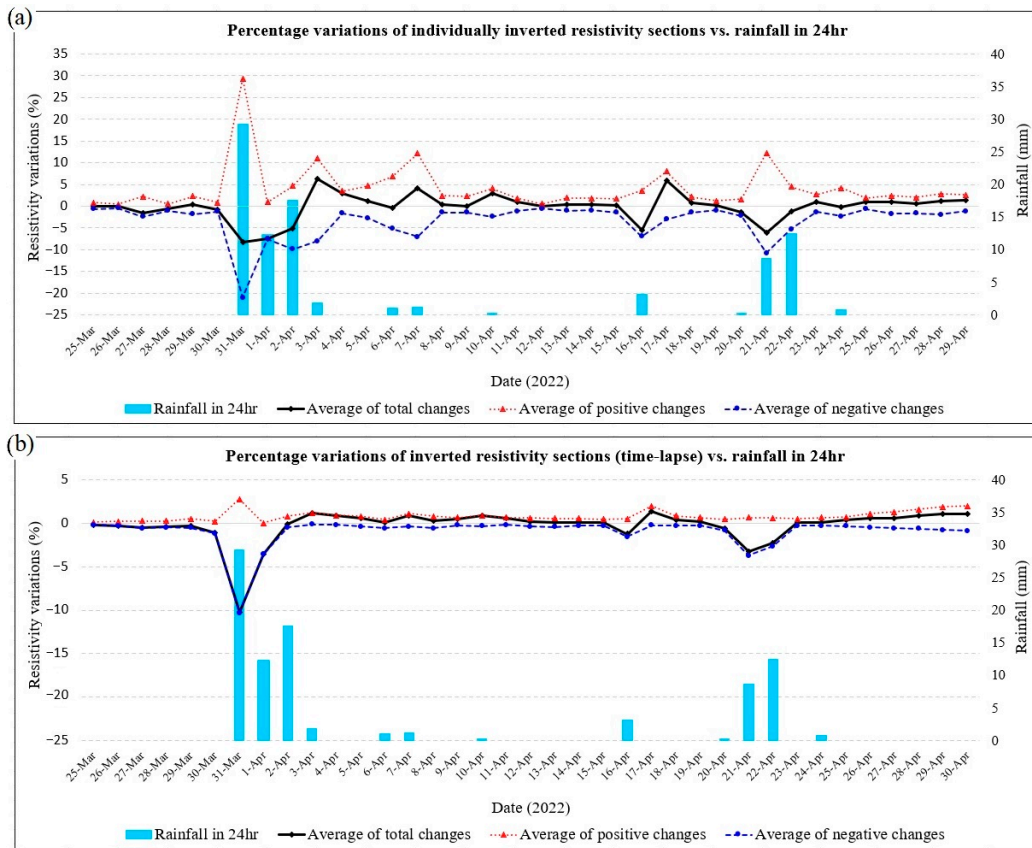
Figure 9. Percentage variations in inverted resistivity sections versus rainfalls in 24 h for the data inverted, applying (**a**) individual inversions, and (**b**) optimized time-lapse inversion.

The benefits of the time-lapse inversions that are synthetically demonstrated by the average resistivities in Figure 9 were also checked in detail by comparing any individual inversion with the corresponding optimized time-lapse inversion. Some examples are illustrated in Figure 10. Figure 10a compares the percentage changes in resistivity values for the data measured on 6 and 7 April, before and after a negligible rainfall (see Figure 9). While the top image in Figure 10a obtained from individual inversions demonstrates unreal positive changes in the central zone approaching a maximum of about 15% and exaggerated negative changes of about 10% in the lateral parts, the bottom image obtained from time-lapse inversions successfully removed these artifacts. Figure 10b presents the example for the data measured before and after a rainfall event that, although not intense, happens after a dry period (see Figure 9) so that we expect negative resistivity changes in the shallow part. In the top image, we can observe artifacts produced by individual inversion that show positive changes mainly in the right part of the ERT line. Applying time-lapse inversion, artifacts of positive changes are eliminated and we observe only realistic negative resistivity changes after the rainfall. Figure 10c reports the example for a heavier rainfall that happens between 20 and 21 April (see Figure 9). The top section obtained from individual inversion suffers again from positive resistivity changes of about 3-13% in the lateral parts while the bottom image is free from positive artifacts and shows only negative resistivity changes due to rainfall infiltration in superficial layers. The last example shown in Figure 10d shows resistivity variations for 25–26 April when no rainfall happens and the subsurface is expected to have a net positive variation due to drying of the layers. This is an opposite situation compared to what we expect after rainfalls. The top image in Figure 10d shows positive resistivity changes in the central zone, but artifacts of negative changes are also present in the lateral parts. Also, in this case, we can observe how

such artifacts are removed in the bottom image when applying a time-lapse algorithm to invert the data. We now observe only positive changes that are reasonably stronger in the very superficial layer. All these examples demonstrate the effectiveness of the calibrated time-lapse inversion algorithm to produce meaningful results that are compatible with external variations, mainly rainfall, in the study site.
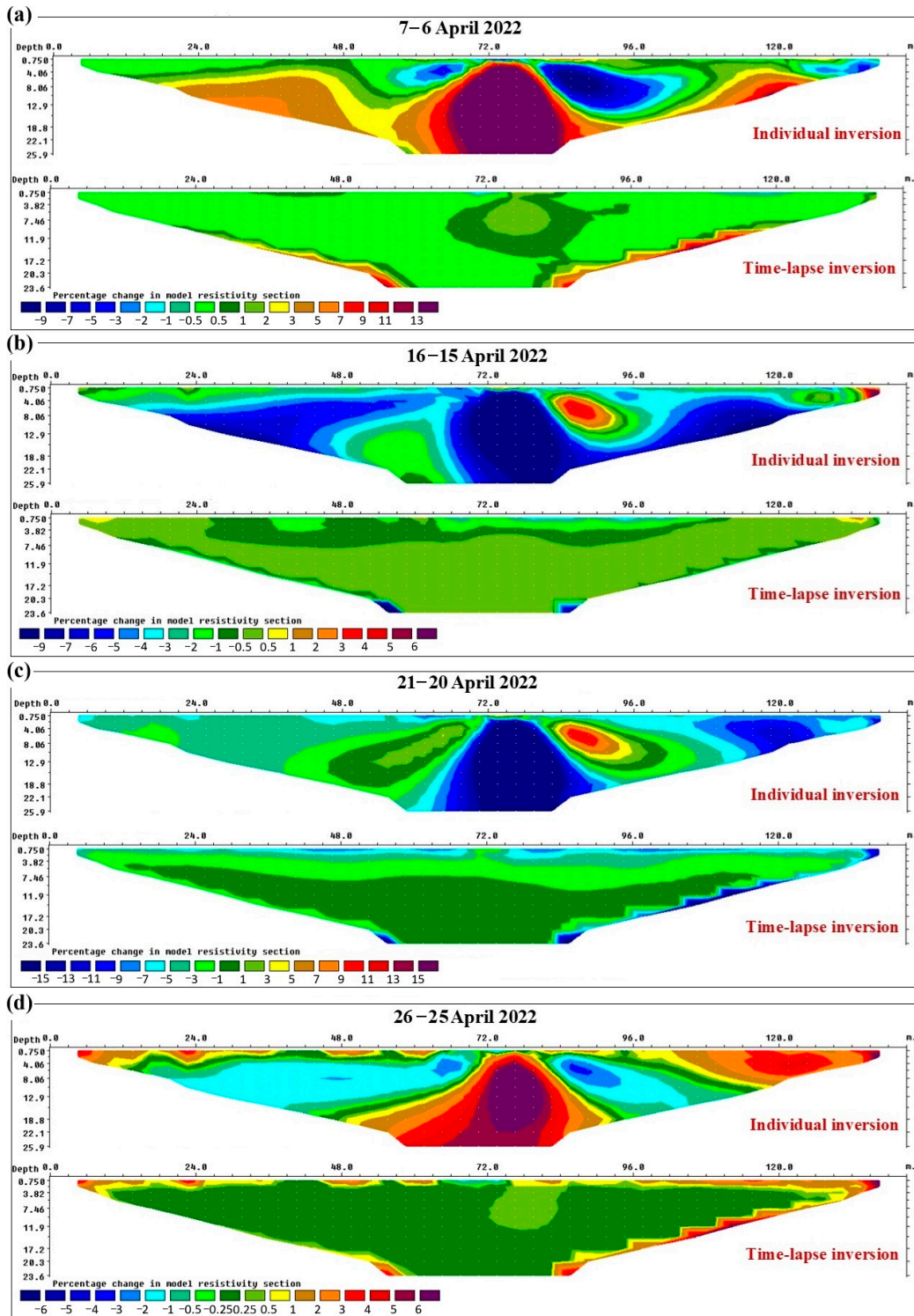

Figure 10. Selected examples of percentage changes in resistivity sections to compare the results obtained from individual inversions with those from time-lapse inversion for the data measured in April 2022.

5. Conclusions

We discussed a long-term ERT monitoring case for which the time-lapse inversions were necessary to prevent artifacts and produce meaningful resistivity models. Forward modeling simulations were necessary to explore the problem and to confirm the nature of the unexpected results, i.e., inversion artifacts produced by individual tomographic inversions. Synthetic tests were also useful to test the effects of the time-lapse inversion parameters. The time-lapse damping factor and the proper norm both for the spatial and the temporal roughness constraint were the most important parameters to be properly calibrated. The simplified synthetic models defined with sharp boundaries were better described using the robust/blocky inversion method for the spatial roughness constraint while the real subsurface with smoother boundaries was better reconstructed using the smooth method in x-z directions. In both cases, the proper norm in the x-z directions could produce resistivity models close to the real situations when combined with the time-lapse damping factor 5 and constraining the time-lapse inversions using the blocky changes in the time direction. The main objective in this paper was to validate the inversion results for the mentioned case study. One future perspective is to apply other inversion methods where the optimal inversion parameters can be automatically optimized and updated during the inversion process [37,41,42] or like the method described in [26] that was applied to a 3D time-lapse dataset. Since the method is guaranteed to eliminate artifacts, it will be interesting to try it on the 2D time-lapse datasets of the case study presented in this paper.

Author Contributions: Conceptualization, A.H., L.Z., G.T., and M.H.L.; methodology, A.H., L.Z., and M.H.L.; software, A.H., L.Z., and M.H.L.; validation, A.H., L.Z., G.T., and M.H.L.; data curation, A.H., L.Z., and M.H.L.; writing—original draft preparation, A.H.; writing—review and editing, A.H., L.Z., G.T., and M.H.L. All authors have read and agreed to the published version of the manuscript.

Data Availability Statement: Data will be available from the corresponding author upon request.

Conflicts of Interest: The authors declare no conflicts of interest.

References

1. Dahlin, T.; Leroux, V.; Larsson, R.; Rankka, K. Resistivity imaging for mapping of quick clays for landslide risk assessment. In Proceedings of the Near Surface 2005, Palermo, Italy, 4–7 September 2005.
2. Chambers, J.E.; Meldrum, P.I.; Gunn, D.A.; Wilkinson, P.B.; Kuras, O.; Weller, A.L.; Ogilvy, R.D. Hydrogeophysical monitoring of landslide processes using automated time-lapse electrical resistivity tomography (ALERT). In Proceedings of the 15th European Meeting of Environmental and Engineering Geophysics, Dublin, Ireland, 7–9 September 2009.
3. Supper, R.; Ottowitz, D.; Jochum, B.; Kim, J.H.; Romer, A.; Baron, I.; Pfeiler, S.; Lovisolo, M.; Gruber, S.; Vecchiotti, F. Geoelectrical monitoring: An innovative method to supplement landslide surveillance and early warning. *Near Surf. Geophys.* **2014**, *12*, 133–150. [CrossRef]
4. Chambers, J.E.; Holmes, J.; Whiteley, J.; Boyd, J.; Meldrum, P.I.; Wilkinson, P.B.; Kuras, O.V.; Swift, R.V.; Harrison, H.; Glendinning, S.; et al. Long-term geoelectrical monitoring of landslides in natural and engineered slopes. *Lead. Edge* **2022**, *41*, 768–776. [CrossRef]
5. Zhang, Z.; Arosio, D.; Hojat, A.; Zanzi, L. Reclassification of microseismic events through hypocentre location: Case study on an unstable rock face in Northern Italy. *Geosciences* **2021**, *11*, 37. [CrossRef]
6. Amitrano, D.; Arattano, M.; Chiarle, M.; Mortara, G.; Occhiena, C.; Pirulli, M.; Scavia, C. Microseismic activity analysis for the study of the rupture mechanisms in unstable rock masses. *Natu Hazards Earth Syst. Sci.* **2010**, *10*, 831–841. [CrossRef]

7.   Watlet, A.; Thirugnanam, H.; Singh, B.; Kumar, N.; Brahmanandan, D.; Inauen, C.; Swift, R.; Meldrum, P.; Uhlemann, S.; Wilkinson, P.; et al. 4D electrical resistivity to monitor unstable slopes in mountainous tropical regions: An example from Munnar, India. *Landslides* **2023**, *20*, 1031–1044. [CrossRef]

8.   Whiteley, J.S.; Chambers, J.E.; Uhlemann, S.; Wilkinson, P.B.; Kendall, J.M. Geophysical monitoring of moisture-induced landslides: A review. *Rev. Geophys.* **2019**, *57*, 106–145. [CrossRef]

9.   Zhang, Z.; Arosio, D.; Hojat, A.; Zanzi, L. Tomographic experiments for defining the 3D velocity model of an unstable rock slope to support microseismic event interpretation. *Geosciences* **2020**, *10*, 327. [CrossRef]

10. Spillmann, T.; Maurer, H.; Green, A.G.; Heincke, B.; Willenberg, H.; Husen, S. Microseismic investigation of an unstable mountainslope in the Swiss Alps. *J. Geophys. Res. Solid Earth* **2007**, *112*, 1–25. [CrossRef]

11. Boyd, J.P.; Binley, A.; Wilkinson, P.; Holmes, J.; Bruce, E.; Chambers, J. Practical considerations for using petrophysics and geoelectrical methods on clay rich landslides. *Eng. Geol.* **2024**, *334*, 107506. [CrossRef]

12. Whiteley, J.; Watlet, A.; Chambers, J.E. Brief communication: The role of geophysical imaging in local landslide early warning systems. *Nat. Hazards Earth Syst. Sci.* **2021**, *21*, 3863–3871. [CrossRef]

13. Bièvre, G.; Oxarango, L.; Günther, T.; Goutaland, D.; Massardi, M. Improvement of 2D ERT measurements conducted along a small earth-filled dyke using 3D topographic data and 3D computation of geometric factors. *J. Appl. Geophys.* **2018**, *153*, 100–112. [CrossRef]

14. Brunet, P.; Clément, R.; Bouvier, C. Monitoring soil water content and deficit using Electrical Resistivity Tomography (ERT)—A case study in the Cevennes area, France. *J. Hydrol.* **2010**, *380*, 146–153. [CrossRef]

15. Feng, L.; Intrieri, E.; Pazzi, V.; Gigli, G.; Tucci, G. A framework for temporal and spatial rockfall early warning using micro-seismic monitoring. *Landslides* **2021**, *18*, 1059–1070. [CrossRef]

16. Schmidt-Hattenberger, C.; Bergmann, P.; Bösing, D.; Labitzke, T.; Möller, M.; Schröder, S.; Wagner, F.; Schütt, H. Electrical resistivity tomography (ERT) for monitoring of CO2 migration—From tool development to reservoir surveillance at the Ketzin pilot site. *Energy Procedia* **2013**, *37*, 4268–4275. [CrossRef]

17. Moradipour, M.; Ranjbar, H.; Hojat, A.; Karimi-Nasab, S.; Daneshpajouh, S. Laboratory and field measurements of electrical resistivity to study heap leaching pad no. 3 at Sarcheshmeh Copper Mine. In Proceedings of the 22nd European Meeting of Environmental and Engineering Geophysics, Barcelona, Spain, 4–8 September 2016. [CrossRef]

18. Hojat, A.; Arosio, D.; Luch, I.D.; Ferrario, M.; Ivanov, V.I.; Longoni, L.; Madaschi, A.; Papini, M.; Tresoldi, G.; Zanzi, L. Testing ERT and Fiber Optic techniques at the laboratory scale to monitor river levees. In Proceedings of the 25th European Meeting of Environmental and Engineering Geophysics, The Hague, The Netherlands, 8–12 September 2019. [CrossRef]

19. Caterina, D.; Orozco, A.F.; Nguyen, F. Long-term ERT monitoring of biogeochemical changes of an aged hydrocarbon contamination. *J. Contam. Hydrol.* **2017**, *201*, 19–29. [CrossRef]

20. Kemna, A.; Vanderborght, J.; Kulessa, B.; Vereecken, H. Imaging and characterisation of subsurface solute transport using electrical resistivity tomography (ERT) and equivalent transport models. *J. Hydrol.* **2002**, *267*, 125–146. [CrossRef]

21. Gance, J.; Malet, J.P.; Supper, R.; Sailhac, P.; Ottowitz, D.; Jochumb, B. Permanent electrical resistivity measurements for monitoring water circulation in clayey landslides. *J. Appl. Geophys.* **2016**, *126*, 98–115. [CrossRef]

22. Kuras, O.; Pritchard, J.D.; Meldrum, P.I.; Chambers, J.E.; Wilkinson, P.; Ogilvy, R.D.; Wealthall, G.P. Monitoring hydraulic processes with automated time-lapse electrical resistivity tomography (ALERT). *Comptes Rendus Geosci.* **2009**, *341*, 868–885. [CrossRef]

23. Carey, A.M.; Paige, G.B.; Carr, B.J.; Doganc, M. Forward modeling to investigate inversion artifacts resulting from time-lapse electrical resistivity tomography during rainfall simulations. *J. Appl. Geophys.* **2017**, *45*, 39–49. [CrossRef]

24. Dahlin, T. Geoelectrical monitoring of embankment dams for detection of anomalous seepage and internal erosion—Experiences and work in progress in Sweden. In Proceedings of the 5th International Conference on Engineering Geophysics (ICEG), Al Ain, United Arab Emirates, 21–24 October 2020. [CrossRef]

25. Tresoldi, G.; Hojat, A.; Zanzi, L.G.R.E.T.A. installations for real-time monitoring of irrigation dams and canals. *Procedia Environ. Sci. Eng. Manag.* **2020**, *7*, 271–276.

26. Loke, M.H.; Wilkinson, P.B.; Chambers, J.E.; Uhlemann, S.; Dijkstra, T.; Dahlin, T. The use of asymmetric time constraints in 4-D ERT inversion. *J. Appl. Geophys.* **2022**, *197*, 104536. [CrossRef]

27. Crawford, M.M.; Bryson, L.S.; Woolery, E.W.; Wang, Z. Long-term landslide monitoring using soil-water relationships and electrical data to estimate suction stress. *Eng. Geol.* **2019**, *251*, 146–157. [CrossRef]

28. Loke, M.H.; Wilkinson, P.B.; Kuras, O.; Meldrum, P.I.; Rucker, D.F. The use of a semi-structured finite-element mesh in 3-D resistivity inversion. *Geophys. Prospect.* **2022**, *70*, 1580–1601. [CrossRef]

29. Loke, M.H.; Acworth, I.; Dahlin, T. A comparison of smooth and blocky inversion methods in 2D electrical imaging surveys. *Explor. Geophys.* **2003**, *34*, 182–187. [CrossRef]

30. deGroot-Hedlin, C.; Constable, S. Occam's inversion to generate smooth, two-dimensional models from magnetotelluric data. *Geophysics* **1990**, *55*, 1613–1624. [CrossRef]

31. Farquharson, C.G.; Oldenburg, D.W. Non-linear inversion using general measures of data misfit and model structure. *Geophys. J. Int.* **1998**, *134*, 213–227. [CrossRef]

32. Vinciguerra, A.; Aleardi, M.; Hojat, A.; Loke, M.H.; Stucchi, E. Discrete cosine transform for parameter space reduction in Bayesian electrical resistivity tomography. *Geophys. Prospect.* **2022**, *70*, 193–209. [CrossRef]

33. Aleardi, M.; Vinciguerra, A.; Stucchi, E.; Hojat, A. Probabilistic inversions of electrical resistivity tomography data with a machine learning-based forward operator. *Geophys. Prospect.* **2022**, *70*, 938–957. [CrossRef]

34. LaBrecque, D.J.; Yang, X. Difference inversion of ERT data: A fast inversion method for 3-D in situ monitoring. *JEEG* **2001**, *6*, 83–89. [CrossRef]

35. Kim, J.H.; Yi, M.J.; Park, S.G.; Kim, J.G. 4-D inversion of DC resistivity monitoring data acquired over a dynamically changing earth model. *J. Appl. Geophys.* **2009**, *68*, 522–532. [CrossRef]

36. Loke, M.H.; Dahlin, T.; Rucker, D.F. Smoothness-constrained time-lapse inversion of data from 3-D resistivity surveys. *Near Surf. Geophys.* **2014**, *12*, 5–24. [CrossRef]

37. Karaoulis, M.; Tsourlos, P.; Kim, J.H.; Revil, A. 4D time-lapse ERT inversion: Introducing combined time and space constraints. *Near Surf. Geophys.* **2014**, *12*, 25–34. [CrossRef]

38. Loke, M.H.; Wilkinson, P.B.; Dahlin, T.; Chambers, J.E.; Uhlemann, S.; Dijkstra, T. Time-lapse 4-D resistivity imaging inversion with positivity constraints. In Proceedings of the Near Surface Geoscience Conference & Exhibition, Porto, Portugal, 9–12 September 2018.

39. Hojat, A. An iterative 3D correction plus 2D inversion procedure to remove 3D effects from 2D ERT data along embankments. *Sensors* **2024**, *24*, 3759. [CrossRef] [PubMed]

40. Geotomosoft Web Portal. Available online: http://geotomosoft.com (accessed on 18 October 2024).

41. Karaoulis, M.C.; Kim, J.H.; Tsourlos, P. 4D active time constrained resistivity inversion. *J. Appl. Geophys.* **2011**, *73*, 25–34. [CrossRef]

42. Kim, J.H.; Supper, R.; Tsourlos, P.; Yi, M.J. Four-dimensional inversion of resistivity monitoring data through Lp norm minimizations. *GJI* **2013**, *195*, 1640–1656. [CrossRef]